Temperature-Dependent Phonon Conduction and Nanotube Engagement in Metalized Single Wall Carbon Nanotube Films

Matthew A. Panzer[1], Hai M. Duong[2], Jun Okawa[3], Junichiro Shiomi[3], Brian L. Wardle[2], Shigeo Maruyama[3], and Ken E. Goodson[1]*

[1]Department of Mechanical Engineering, Stanford University, Stanford, California 94305

[2]Department of Aeronautics and Astronautics, Massachusetts Institute of Technology, Cambridge, Massachusetts 02139

[3]Department of Mechanical Engineering, University of Tokyo, Tokyo 113-8656, Japan

mpanzer@stanford.edu

Corresponding author: Address: Department of Mechanical Engineering, 440 Escondido Mall, Stanford University, Stanford, CA 94305; Tel. 650 725 2086; Fax 650 723 7657; email: goodson@stanford.edu

Interfaces dominate the thermal resistance parallel to aligned carbon nanotube arrays. This work uses nanosecond thermoreflectance thermometry to separate interface and volume resistances for 10 μm thick aligned SWNT films coated with Al, Ti, Pd, Pt, and Ni. We interpret the data by defining the nanotube-metal engagement factor, which governs the interface resistance and is extracted using the measured film heat capacity. The metal-SWNT and SWNT-substrate resistances range between 3.8-9.2 mm^{2}K/W and

33-46 mm²K/W, respectively. The temperature dependency of the heat capacity data, measured between 125-300 K, is in good agreement with theoretical predictions. The temperature dependence demonstrated by the metal-SWNT interface resistance data suggests inelastic phonon transmission.

Aligned arrays of single and multi-wall carbon nanotubes (SWNT, MWNT) films are promising materials for thermal management[1-4] and electronics applications such as field emission devices,[5] flexible electronics,[5] transistors,[6] sensors,[7] tough interfaces,[8] and energy storage materials.[9] They potentially offer the unique combination of low thermal resistance and controllable elastic modulus due to the high thermal conductivity (>3000 $Wm^{-1}K^{-1}$)[10,11] and flexibility of individual nanotubes.[12,13] However, integrating these materials into devices and structures creates additional interfaces, often with metals, that inhibit heat conduction.

Measurements with various nanotube-substrate interface combinations such as pressed metal and dielectric interfaces,[1,2,4] growth interfaces,[3,4,14,15] and physically deposited metals,[3,15] yield large nanotube-substrate thermal interface resistances in the range of 0.3-50 mm²K/W. These large resistances are due to incomplete nanotube-substrate contact amplifying the nanoscale conduction resistances of individual nanotube-substrate interfaces.[3,15] Such individual nanoscale metal-tube interfaces often dominate the conduction resistances for film thicknesses below ~50 μm. The nanoscale features of the contact further complicate the interface resistance by modifying the phonon transport physics, for which there are no established models.[16] The structure of these interfaces at the nanoscale is highly dependent on the interaction, adhesion, and wettability of the CNT and substrate materials. Previous data yield no clear relation between interface resistance and interface structure. Better understanding the contribution of the interface materials on the conduction physics and effective nanotube contact area at the interface are necessary to improve the thermal performance of nanotube films. This work directly measures the contribution of interface metallization on the SWNT engagement efficiency and thermal interface resistances via the composition dependence of the interface resistances and effective heat capacities of

metal-coated SWNT films using nanosecond thermoreflectance thermometry. The temperature dependence of these properties provides a means to study phonon transmission at the interface.

The details of the alcohol-CVD SWNT growth process used in this work can be found in Murakami et al.[17] Dip-coating a Si substrate into a Co-Mo acetate solution forms a dispersed monolayer of catalyst particles ($\sim 1.3 \times 10^{17}$ m^{-2}). Annealing in air at 400 °C converts the acetates to metal oxides, followed by an Ar/H$_2$ reducing flow to retrieve the catalytic activity. The SWNTs are grown using alcohol-CVD at 800 °C[17] to yield an aligned SWNT film 10 μm thick and a SWNT density of ~2-3% (estimated from mass measurements). Raman data yield an average SWNT diameter of 1.9 nm and a D/G ratio of 0.012 with a D-band FWHM of 20 cm^{-1}, suggesting high purity films. TEM images reveal that the SWNT films consist of SWNT bundles with ~10 or fewer nanotubes per bundle and a median of 6 SWNTs per bundle.[18] The resolution limits of the TEM place a lower bound of ~10% on the number of bundles that consist of individual tubes; however, the actual number may be much larger. Aligned SWNT films are individually metalized by e-beam evaporating a 50 nm coating of either Al, Pt, Pd, Ti, or Ni at a substrate temperature of ~300 K. SEM images of the individual samples were used to measure the local SWNT thicknesses, and showed thickness variations less than 1.0 μm. Following an air break, 50 nm of Al was e-beam evaporated onto the samples to improve the surface reflectivity and uniformity for the thermoreflectance measurement. Duong et al.[19] present a detailed SEM analysis of the dependence of the metal-SWNT morphology on material and deposition conditions. A representative TEM cross section of an Al(160 nm)/Pd(20 nm)-SWNT interface in Fig. 1a shows many voids and a lower SWNT density near the interface compared to deeper within the sample. This incomplete contact leads to partial engagement between the SWNTs and the metal, increasing thermal conduction resistances.
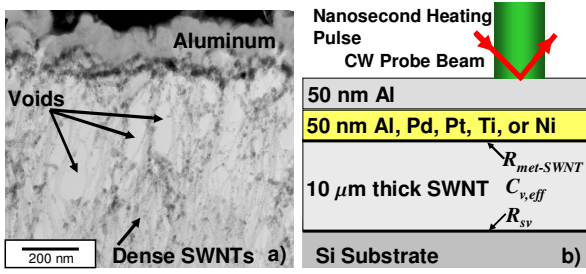
Figure 1. a) Representative TEM of SWNT-metal contact showing voids and incomplete contact near the metal interface. b) Schematic of sample geometry used in the measurements and for the thermal model.

This study uses nanosecond thermoreflectance thermometry to measure the interface resistances and heat capacity of the metalized SWNT films, the details of which can be found in previous work.[3] In brief, a 3 mm diameter, 532 nm wavelength, 6 ns pulse from a Nd:YAG laser heats the surface of the metal film at a rep-rate of 10 Hz. A 10 mW, 658 nm continuous wave probe laser is focused on the metal in the middle of the pump beam to a diameter of ~20 μm. A 650 MHz photodiode and oscilloscope capture the reflected intensity of the probe laser with sub-μs temporal resolution. The reflected probe intensity linearly tracks the relative changes in metal surface temperature, yielding the normalized thermal response. Lateral heat conduction is negligible since the pump beam diameter is much large than the maximum thermal diffusion distance during the measurement.

A least-squares algorithm fits the data to a solution of the heat diffusion equation for a multilayered stack model of the structure (Fig. 1b) using three parameters:[3] the metal-SWNT interface resistance, $R_{met\text{-}SWNT}$, the effective volumetric heat capacity of the SWNT film, $C_{v,eff}$, and a resistance, $R_{sv}=R_{SWNT\text{-}sub}+R_{SWNT,vol}$, which captures the combined resistance of the SWNT-substrate interface resistance ($R_{SWNT\text{-}sub}$) and the residual volumetric resistance of the SWNT film ($R_{SWNT,vol}$). The measurement for these particular samples is sensitive only to R_{sv} and neither $R_{SWNT\text{-}sub}$ nor $R_{SWNT,vol}$ individually. The unique impact of $R_{met\text{-}SWNT}$, $C_{v,eff}$, and R_{sv} on the shape of the thermal response at different time scales permits their isolation.[3] The effective SWNT volume fraction contributing to the

heat capacity can be estimated by $\phi = C_{v,eff}/C_{v,ind}$, where $C_{v,ind} \sim 1.5$ MJ/m^{3}K^{-1} is the volumetric heat capacity of an individual SWNT.[3] In fitting the data, we assume an effective SWNT conductivity of $k_{cnt,eff} = \phi \times k_{SWNT}$, where $k_{SWNT} = 3600$ Wm^{-1}K^{-1} is the individual SWNT thermal conductivity.[10] We neglect the metal-metal interface resistance since it is typically much less than $R_{met\text{-}SWNT}$, and since the thermalization time of the metals is less than the temporal resolution of the system.

Figure 2a plots $R_{met\text{-}SWNT}$, R_{sv}, and their sum total, R_{tot}, versus the measured effective heat capacity volume fraction, ϕ, for the five metallization. The error bars capture the uncertainty due to variations in measurement data taken at four different locations on each sample, variations in film physical properties (e.g. film thickness), and the sensitivity to the uniqueness of the fit parameter combinations. While $R_{met\text{-}SWNT}$ falls in the range of 3.5-9.2 mm^{2}K/W, R_{sv} is much larger, ranging between 33-46 mm^{2}K/W. Attributing these larger values of R_{sv} to $R_{SWNT,vol}$ would require a very low value of $k_{cnt,eff} \approx 0.3$ Wm^{-1}K^{-1}, which would yield an estimate of $k_{SWNT} \approx 45$ Wm^{-1}K^{-1} based on the effective SWNT volume fraction, ϕ. Since this value seems rather low given the high quality of the SWNT tubes indicated by the Raman data, we suggest that a more plausible explanation is that the large R_{sv} is dominated by $R_{SWNT\text{-}sub}$ due to the weak adhesion of the catalyst particles resulting from the "dip-coating" technique. Measurements of similar films[3] that utilized PVD catalyst deposition showed similar values for $R_{met\text{-}SWNT}$, but much lower values of $R_{SWNT\text{-}sub}$ at a lower ϕ.
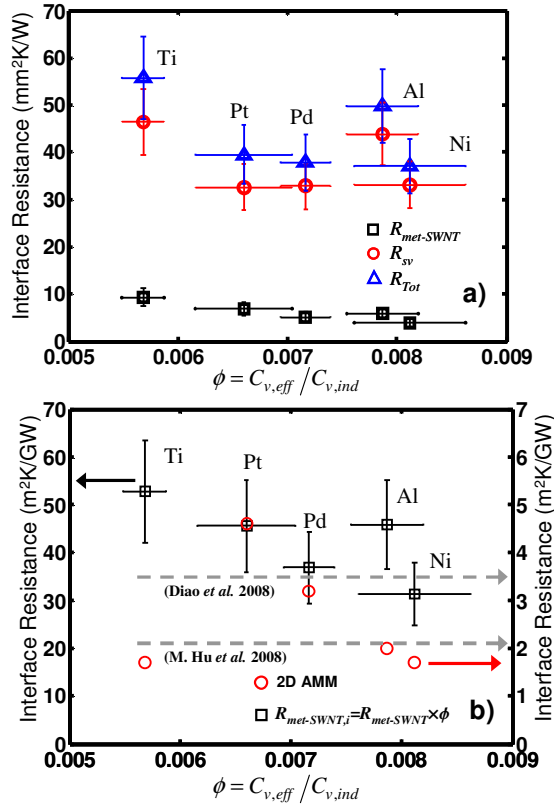
Figure 2. a) Measured area-averaged metal-SWNT, SWNT-substrate, and total thermal resistance plotted as a function of the measured effective SWNT heat capacity volume fraction, ϕ, calculated by dividing the measured effective SWNT volumetric heat capacity $C_{v,eff}$, by the volumetric heat capacity of an individual SWNT, $C_{v,ind}$. b) Estimated resistance of individual metal-SWNT contact extracted by multiplying the area-average metal-SWNT interface resistance by ϕ. Data are compared to theoretical predictions of the individual SWNT interface resistance from molecular dynamics of SWNT-Si interfaces from M. Hu et al.[20] and Daio et al.[21] (gray-dashed arrows) and from the AMM model modified for 2D-2D interfaces.[3] The theoretical values are shown on the right axis for clarity.

The observations that the effective SWNT volume fractions are much less than the nominal volume fraction of 3%, and the trend in the data of decreasing $R_{met\text{-}SWNT}$ with increasing ϕ suggest that the large interface resistance in SWNT arrays are due to a low SWNT engagement efficiency with the metal. Sample-dependent nanoscale surface morphologies and differences between the metals' abilities to coat

the SWNTs may explain their relative engagement efficiencies. Previous observations[19,22] showed that the metal-SWNT coating behavior can be strongly dependent on metal-SWNT interaction energies,[22] with Ti, Ni, Pd, and Al demonstrating an increasing tendency to cluster on the individual SWNTs. Metals that effectively coat the SWNTs can show reduced engagement due to the lower tendency of the metal to form inter-tube clusters that can bridge multiple tubes and bundles. This effect can explain the low value of ϕ for Ti compared to other metals since Ti has an excellent ability to coat SWNT and a low tendency to form clusters.

The thermal resistance of an individual SWNT-metal interface, $R_{met-SWNT,i}$, can be estimated from the relation $R_{met-SWNT,i} = R_{met-SWNT} \times \phi$.[3] Fig. 2b shows the relation between $R_{met-SWNT,i}$ and ϕ, along with the results of molecular dynamics simulations for the resistance of an individual (10,10) SWNT-Si interface.[20,21] Fig. 2b also shows theoretical predictions of individual metal-SWNT interface resistances based on a modification of the acoustic mismatch model (AMM) in an approximation treating the SWNT as a graphene-metal 2D-2D interfaces.[3] The AMM model predicts resistances similar to the molecular dynamics (MD) simulations of Si-SWNT interfaces and follows the general data trend with metallization.

The trend of decreasing $R_{met-SWNT,i}$ with increasing ϕ suggests that the same physical properties that govern the interface resistance (e.g. interface adhesion energies, Debye temperatures, etc.) may be related to the mechanisms that govern the engagement of the metal with the SWNTs. $R_{met-SWNT,i}$ is about an order of magnitude larger than the theoretical predictions. Non-ideal metal-SWNT interface geometries may explain this discrepancy. The bundle structure of the nanotubes can reduce the ratio of the metal-SWNT interface area to the SWNT volume and consequently increase the apparent individual metal-SWNT interface resistance. The models do not account for the likely formation of metal nanoclusters along the SWNTs which creates additional interfaces and modifies the local phonon density of states due to the effects of reduced and mismatched geometries.[23-25] However, the lower interface resistance values predicted by the MD simulations suggest that in addition to improving the engagement,

there is the potential to significantly reduce the thermal resistance of SWNT films by reducing the individual metal-SWNT interface resistance.

Figure 3a,b is a plot of the temperature dependence of $C_{v,eff}$ and the interface conductance per tube, $(R_{met-SWNT} \times \phi)^{-1}$ and $(R_{sv} \times \phi)^{-1}$, between 125 K and 300 K for a 10 μm thick SWNT film coated with a 100 nm thick aluminum film. The temperature dependencies of these data can provide information about the phonon conduction physics. Optimal power law fits to the data yield temperature dependencies of $C_{v,eff} \sim T^{0.97}$, $(R_{met-SWNT})^{-1} \sim T^{1.08}$, and $(R_{sv})^{-1} \sim T^{0.85}$. In considering the phonon properties, the bundling does not influence the temperature dependences of $C_{v,eff}$ since $k_b T >> E_{d\perp}$, where $E_{d\perp} \sim 5$ meV is the Debye energy of the intertube coupling modes and k_b is Boltzman's constant.[26] The SWNT thermal properties are well approximated by those of graphene since $\theta_{sub} << T$ where $\theta_{sub} \sim 10$ K is the characteristic temperature of the first optical sub-band of the SWNT estimated from calculations using the dynamical matrix of a classical potential field.[26,27] Fig. 3a compares the measured data to theoretical calculations of the heat capacity of an individual 2 nm diameter SWNT tube using Bose-Einstein statistics based on the above dynamical matrix, and a calculation of the total heat capacity of the acoustic phonon modes in graphene using the band parameters in Prasher et al.[28] Fig. 3a shows the individual contribution of the longitudinal acoustic (LA), transverse acoustic (TA), and out-of-plane bending modes (ZA) of graphene to its total heat capacity. Due to the porosity of the SWNT film, the theoretical calculations have been scaled by a factor of 0.006 so that the calculation of the heat capacity matches the experimental data at 300 K. Note that, despite its empirical nature, the classical potential field[27] reproduces the overall features of the phonon dispersion to an extent sufficient for the current analysis.[29] The temperature dependency of the experimental data follows the theoretical predictions of the heat capacity calculation of the SWNT within the measurement uncertainty. The near identical temperature dependency of the acoustic mode heat capacity of graphene and that of the SWNT suggest that the thermal properties of the SWNT are well captured by phonon physics of graphene, in the current temperature range. The calculations show that although the heat capacity is dominated by the ZA mode, the temperature

dependency of the LA and TA modes is stronger in this temperature regime, resulting in a temperature scaling of the total heat capacity that is strongly influenced by all modes.
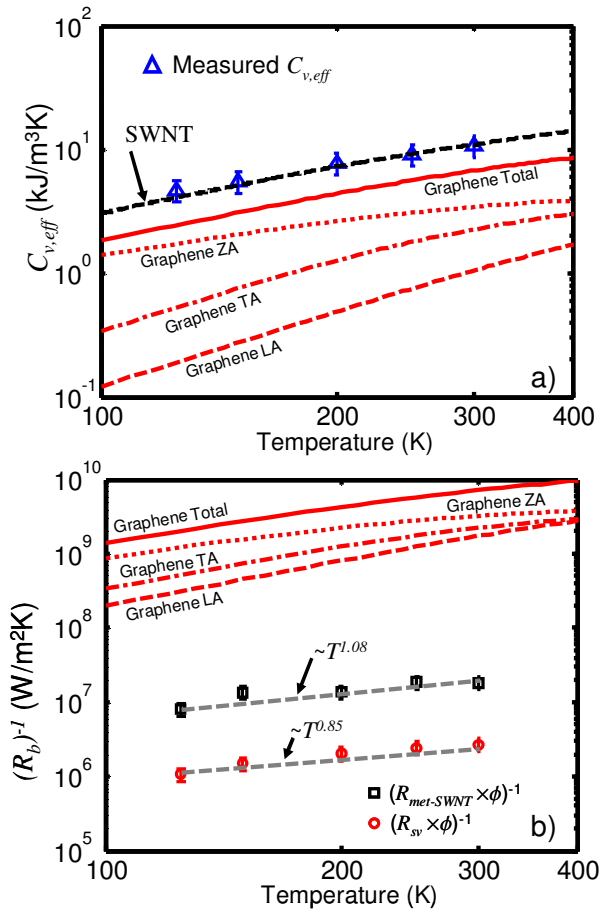

Figure 3. a) Temperature dependence of the area-average metal-SWNT interface and effective $C_{v,eff}$ for a 100 nm-thick Al-coated SWNT film. The data are compared to theoretical calculation of the heat capacity of an individual SWNT based on Bose-Einstein statistics using a classical potential function[27] (black-dashed) and a calculation of the heat capacity of graphene acoustic modes (red-solid) based on graphene parameters in Prasher et al.[28] The theoretical predictions have been scaled by a factor of 0.006 so that the value of the data matches the SWNT theoretical results at 300 K. Also shown are the contributions of the graphene longitudinal (LA), transverse (TA), and out-of-plane bending (ZA) acoustic phonon bands to the total graphene heat capacity. b) Temperature dependence of the conductance of individual SWNT interfaces, $(R_{met-SWNT} \times \phi)^{-1}$ and $(R_{sv} \times \phi)^{-1}$. The gray dashed curves are optimal power law fits to the data. The solid red curve is the total theoretical upper bound for the

interface conductance of a graphene-metal interface allowing for inelastic scattering. The broken red curves show the contributions from the individual acoustic phonon modes in graphene.

The temperature dependence of $R_{met\text{-}SWNT}$ yields information about the metal-SWNT phonon interface transmittance. Under the assumption of a small temperature difference across the interface and isotropic phonon dispersion, the boundary resistance can be expressed as[30,31]

$$R_b^{-1} = \Gamma^{inel}(T) \sum_s \frac{1}{\Omega_d} \int_{\Omega_d^+} \int_0^{\omega_{max,s}} \hbar \omega v_s(\omega) \cos(\theta) \frac{\partial n}{\partial T} g_s(\omega) d\omega d\Omega_d \tag{1}$$

where s is the mode branch, ω is the phonon frequency, $v_s(\omega)$ is the phonon velocity, n is the Bose-Einstein distribution, T is the temperature, $g_s(\omega)$ is the phonon spectral density of states, θ is the angle between $\vec{k}$, the phonon wave vector, and the interface normal, Ω_d is the solid angle for d-dimensional space. $\Gamma^{inel}(T)$ is the net phonon transmittance, which allows for implicit inelastic phonon scattering at the interface.[31] The integral is taken over the half space of phonons directed toward the interface (Ω^+). To predict the temperature dependency of the interface conductance of the SWNT, we evaluate Eq. (1) using the acoustic bands of graphene since the temperature dependency of the phonon heat capacity is well approximated by that of graphene for the temperature range in this work (Fig. 3a). Evaluating Eq. (1) from the graphene (SWNT) side of the of the interface and equating $\omega_{max,s}$ to the Debye frequencies of the graphene acoustic modes (which are greater than those of Al) implicitly allows for inelastic phonon transmission.[31] Setting $\Gamma^{inel}(T) = 1$ provides the upper limit to the total (inelastic and elastic) phonon conductance. Assuming a general dispersion relation of the form $\omega_s = c_s k^\alpha$ and combining with Eq. (1) yields

$$R_b^{-1} = \Gamma^{inel}(T) \sum_s \frac{k_b \Omega_d}{(2\pi)^d} \left(\frac{1}{c_s}\right)^{\frac{d-1}{\alpha}} \left(\frac{k_b T}{\hbar}\right)^{\frac{d-1}{\alpha}+1} \int_0^{\frac{\hbar \omega_{max,s}}{k_b T}} \frac{x^{\frac{d-1}{\alpha}+2} e^x dx}{(e^x - 1)^2} \tag{2}$$

where d is the dimension. Fig. 3b shows the evaluation of Eq. (2) using the properties of graphene for the upper bound ($\Gamma^{inel}(T) = 1$) of the total interface conductance and the individual contributions from the LA, TA, and ZA graphene modes. As with the heat capacity, the interface conductance is dominated by

the ZA mode, but the temperature dependency of the LA and TA modes is stronger in this temperature regime, resulting in a temperature scaling of the interface conductance that is strongly influenced by all acoustic modes.

Fig. 4 shows the temperature dependence of $\Gamma^{inel}(T)$ extracted by dividing the experimental data for the per tube interface conductance by Eq. (2) evaluated with $\Gamma^{inel}(T) = 1$. A power law fit to the data yields $\Gamma^{inel}(T) \sim T^n$ where $0.4 < n < 0.9$ with an optimal of $n \sim 0.6$. Since traditional AMM and diffuse mismatch models (DMM) in the Debye approximation with elastic scattering[32] result in $\Gamma^{inel}(T) \sim T^0$ with values on the order of unity, the data suggest that these simpler models do not fully capture the physics of the transport across metal-SWNT interfaces. The low values of Γ^{inel} may be due non-ideal interface geometry, multiple interfaces in series within the SWNT bundles, and metal clusters along the SWNT amplifying the interface resistance.
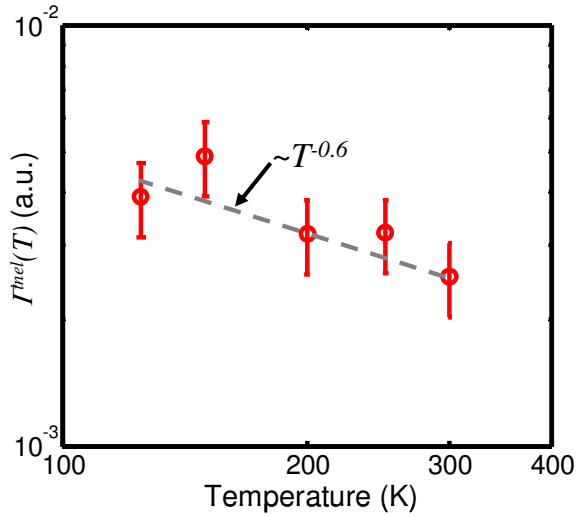

Figure 4. Temperature dependence of $\Gamma^{inel}(T)$ along with the optimal power law fit (gray-dashed). The temperature dependence suggests inelastic phonon scattering at the interface.

The temperature dependence of $\Gamma^{inel}(T)$ suggests a spectral dependence of the individual phonon mode transmission coefficients. This dependency may be due to a combination of inelastic phonon scattering at the interface and density of states mismatch between the materials,[33] which can be complicated by the

nanoscale geometry,[23-25] and interface disorder.[34] Inelastic interface scattering becomes more important as the temperature approaches the lower Debye temperature of the two materials. Previous measurements of the boundary resistances of Al/sapphire,[35,36] Pb/diamond,[37] and Au/diamond[31,38] all reported near-linear trends in the boundary conductance over similar temperature ranges, which were attributed to inelastic scattering. Hopkins et al.[31] reported a decreasing $\Gamma^{inel}(T)$ with increasing temperature due to inelastic scattering. These similar trends in the temperature dependency of $R_{met\text{-}SWNT}$ and $\Gamma^{inel}(T)$ indicates that inelastic scattering may be important at metal-SWNT interfaces.

In summary, we find that the thermal interface resistances in SWNT films are much larger than the volumetric contribution. These resistances are controlled by the degree of engagement of the SWNT films by the metal and the nanoscale interface resistances. Improving the nanotube-metal contact can potentially reduce the total thermal resistances of nanotube arrays below 1 mm^{2}K/W, allowing the volumetric thermal conduction of the CNTs to dominate.

(1) Xu, J.; Fisher, T. S. *Int. J. of Heat and Mass Transfer* **2006**, *49*, 1658-1666.

(2) Hu, X. J.; Padilla, A. A.; Xu, J.; Fisher, T. S.; Goodson, K. E. *J. Heat Transfer* **2006**, *128*, 1109-1113.

(3) Panzer, M. A.; Zhang, G.; Mann, D.; Hu, X.; Pop, E.; Dai, H.; Goodson, K. E. *J. Heat Transfer* **2008**, *130*, 052401-9.

(4) Cola, B. A.; Xu, J.; Cheng, C.; Xu, X.; Fisher, T. S.; Hu, H. *J. of Appl. Phys.* **2007**, *101*, 054313-9.

(5) Tsai, T. Y.; Lee, C. Y.; Tai, N. H.; Tuan, W. H. *Appl. Phys. Lett.* **2009**, *95*, 013107-3.

(6) Cao, Q.; Zhu, Z.-T.; Lemaitre, M. G.; Xia, M.-G.; Shim, M.; Rogers, J. A. *Appl. Phys. Lett.* **2006**, *88*, 113511-3.

(7) Modi, A.; Koratkar, N.; Lass, E.; Wei, B.; Ajayan, P. M. *Nature* **2003**, *424*, 171-174.

(8) Garcia, E. J.; Wardle, B. L.; John Hart, A. *Comp. A* **2008**, *39*, 1065-1070.

(9) Chen, J.; Liu, Y.; Minett, A. I.; Lynam, C.; Wang, J.; Wallace, G. G. *Chem. Mat.* **2007**, *19*, 3595-3597.

(10) Pop, E.; Mann, D.; Wang, Q.; Goodson, K.; Dai, H. *Nano. Lett.* **2006**, *6*, 96-100.

(11) Kim, P.; Shi, L.; Majumdar, A.; McEuen, P. L. *Phys. Rev. Lett.* **2001**, *87*, 215502.

(12) Iijima, S.; Brabec, C.; Maiti, A.; Bernholc, J. *J. Chem. Phys.* **1996**, *104*, 2089-2092.

(13) Yaglioglu, O.; Martens, R.; Hart, A. J.; Slocum, A. H. *Adv. Mater.* **2008**, *20*, 357-362.

(14) Son, Y.; Pal, S. K.; Borca-Tasciuc, T.; Ajayan, P. M.; Siegel, R. W. *J. of Appl. Phys.* **2008**, *103*, 024911-7.

(15) Tong, T.; Zhao, Y.; Delzeit, L.; Kashani, A.; Meyyappan, M.; Majumdar, A. *IEEE Transactions on Components and Packaging Technologies* **2007**, *30*, 92-100.

(16) Duong, H. M.; Yamamoto, N.; Papavassiliou, D. V.; Maruyama, S.; Wardle, B. L. *Nanotechnology* **2009**, *20*, 155702.

(17) Murakami, Y.; Miyauchi, Y.; Chiashi, S.; Maruyama, S. *Chem. Phys. Lett.* **2003**, *377*, 49-54.

(18) Einarsson, E.; Shiozawa, H.; Kramberger, C.; Rummeli, M. H.; Gruneis, A.; Pichler, T.; Maruyama, S. *J. Phys. Chem. C* **2007**, *111*, 17861-17864.

(19) Duong, H. M.; Ishikawa, K.; Okawa, J.; Ogura, K.; Einarsson, E.; Shiomi, J.; Maruyama, S. *J. Phys. Chem. C* **2009**, *113*, 14230-14235.

(20) Hu, M.; Keblinski, P.; Wang, J.-S.; Raravikar, N. *J. Appl. Phys.* **2008**, *104*, 083503-4.

(21) Diao, J.; Srivastava, D.; Menon, M. *J. of Chem. Phys.* **2008**, *128*, 164708-5.

(22) Zhang, Y.; Franklin, N. W.; Chen, R. J.; Dai, H. *Chemical Physics Letters* **2000**, *331*, 35-41.

(23) Panzer, M. A.; Goodson, K. E. *J. of Appl. Phys.* **2008**, *103*, 094301-10.

(24) Prasher, R.; Tong, T.; Majumdar, A. *J. Appl. Phys.* **2007**, *102*, 104312-10.

(25) Zhang, W.; Mingo, N.; Fisher, T. S. *Phys. Rev. B* **2007**, *76*, 195429-9.

(26) Hone, J.; Batlogg, B.; Benes, Z.; Johnson, A. T.; Fischer, J. E. *Science* **2000**, *289*, 1730-1733.

(27) Brenner, D. W. *Phys. Rev. B* **1990**, *42*, 9458.

(28) Prasher, R. *Phys. Rev. B* **2008**, *77*, 075424-11.

(29) Shiomi, J.; Maruyama, S. *Phys. Rev. B* **2006**, *73*, 205420.

(30) Lisa De Bellis, P. E. P., Ravi S. Prasher *J. Thermophys. and Heat Trans.* **2000**, *14*, 144-150.

(31) Hopkins, P. E.; Norris, P. M. *J. Heat Transfer* **2009**, *131*, 022402-9.

(32) Schwartz, E.; Pohl, R. *Rev. Mod. Phys.* **1989**, *61*, 605-668.

(33) Phelan, P. E. *J. Heat Transfer* **1998**, *120*, 37-43.

(34) Stevens, R. J.; Zhigilei, L. V.; Norris, P. M. *Int. J. of Heat and Mass Trans.* **2007**, *50*, 3977-3989.

(35) Stoner, R. J.; Maris, H. J. *Physical Review B* **1993**, *48*, 16373.

(36) Hopkins, P. E.; Norris, P. M.; Stevens, R. J. *J. Heat Transfer* **2008**, *130*, 022401-9.

(37) Lyeo, H.-K.; Cahill, D. G. *Phys. Rev. B* **2006**, *73*, 144301-6.

(38) Hopkins, P.; Salaway, R.; Stevens, R.; Norris, P. *Int. J. of Thermophysics* **2007**, *28*, 947-957.

Table of Contents Figure